Journal of Materials Chemistry A

PAPER

View Article Online
View Journal | View Issue

Cite this: J. Mater. Chem. A, 2015, 3, 5608

Dual template-directed synthesis of SAPO-34 nanosheet assemblies with improved stability in the methanol to olefins reaction†

Chan Wang,[abc] Miao Yang,[ab] Peng Tian,[ab] Shutao Xu,[ab] Yue Yang,[ab] Dehua Wang,[abc] Yangyang Yuan[abc] and Zhongmin Liu*[ab]

Received 12th November 2014
Accepted 28th January 2015

DOI: 10.1039/c4ta06124a

www.rsc.org/MaterialsA

A spherical self-assembly of SAPO-34 nanosheets was hydrothermally synthesized by using a quaternary ammonium-type organosilane surfactant [3-(trimethoxysilyl)propyl]octadecyldimethylammonium chloride (TPOAC) as the mesoporogen and a part of the silica source, and diethylamine (DEA) as the microporous template. The prepared materials were well characterized by XRD, XRF, SEM, TEM, N_2 adsorption–desorption, NH_3-TPD, NH_3-adsorbed IR and pyridine-adsorbed IR measurements. It revealed that the morphologies, compositions and acidity of the SAPO-34 products changed significantly with the increased TPOAC/TEOS ratio, showing that the TPOAC/TEOS ratio had a significant impact on the crystallization process of SAPO-34. Solid state ^{13}C, ^{29}Si NMR and TG-DTA analyses were further conducted to investigate the status of TPOAC in the final products. A possible crystallization process involving TPOAC was proposed. The catalytic performances of the synthesized SAPO-34s were evaluated using the MTO reaction. The optimal SAPO-34 nanosheet assemblies with a hierarchical porous structure displayed a remarkably enhanced catalytic lifetime and high yields of light olefins.

1 Introduction

Silicoaluminophosphate (SAPO) molecular sieves, invented by Union Carbide Corporation in the 1980s, are important crystalline materials.[1–4] Incorporation of silicon atoms into the neutral $AlPO_4$ lattice generates acidity, which gives SAPO molecular sieves many significant applications as catalysts, catalyst supports and adsorbents.[5–9] SAPO-34 with a CHA topology is one of the most investigated silicoaluminophosphate molecular sieves due to its excellent performance in the methanol-to-olefin (MTO) reaction (100% methanol conversion and over 90% selectivity to C_2–C_4 light olefins).[10–12] Unfortunately, the small 8-ring pore opening (3.8 × 3.8 Å) and large CHA cavity (9.4 Å in diameter) structure cause a severe diffusion limitation resulting in rapid deactivation by coke deposition during the MTO process. It is highly desirable to improve the stability of the SAPO-34 catalyst without sacrificing its inherent selectivity and catalytic activity.

Considerable efforts have been made to optimize the SAPO-34 catalyst,[13–17] and integration of meso- or/and macropores into the microporous structures is considered as an attractive solution. Wei *et al.* obtained hierarchical SAPO-34 composed of decussate zeolite slice units by using natural layered kaolin as a special Si and Al source.[14] The enhanced conversion and olefin selectivity in the dimethyl ether to olefin reaction are attributed to the unique hierarchical structure. Xie *et al.* prepared a hierarchical SAPO-34 monolith through a dry gel conversion of the amorphous silicoaluminophosphate monolith.[18] Schmidt *et al.* synthesized hierarchical SAPO-34 by using carbon materials as hard templates.[19] Yu *et al.* prepared the hierarchically macroporous SAPO-34 by using an *in situ* growth-etching approach.[20] It is surprising that although the soft-template directing method is very popular in the synthesis of mesoporous aluminosilicate zeolites,[21–25] it is not well developed to synthesize mesoporous aluminophosphate and silicoaluminophosphate molecular sieves. Progress has been made in the synthesis of mesoporous SAPO-34 by using certain polymers as mesopore-directing agents,[26,27] but obtaining a high-quality silicoaluminophosphate catalyst with uniform mesopores through this method still poses many challenges. Quaternary ammonium-type organosilane surfactants are one class of the most promising mesopore-generating agents for the synthesis of mesoporous zeolites. They can simultaneously act as parts of the silica source and mesoporogens during the synthesis, preventing the phase separation of zeolites and mesoporous materials.[21,28,29] By using 3-(trimethoxysilyl)propyl hexadecyldimethylammonium chloride ($[(CH_3O)_3SiC_3H_6N(CH_3)_2C_{16}H_{33}]Cl$, TPHAC), Ryoo *et al.* successfully synthesized mesoporous AlPO-5, AlPO-11 and SAPO-5;

[a]Dalian National Laboratory for Clean Energy, Dalian Institute of Chemical Physics, Chinese Academy of Sciences, Dalian, P. R. China. E-mail: liuzm@dicp.ac.cn

[b]National Engineering Laboratory for Methanol to Olefins, Dalian Institute of Chemical Physics, Chinese Academy of Sciences, Dalian, P. R. China

[c]University of Chinese Academy of Sciences, Beijing, P. R. China

† Electronic supplementary information (ESI) available. See DOI: 10.1039/c4ta06124a

however, hierarchical SAPO-5 lacks strong acid sites, though a high silica content (molar composition of $Al_{0.50}P_{0.14}Si_{0.36}O_2$) is claimed.[30] In 2010, Wang *et al.* synthesized hierarchical SAPO-34 with [3-(trimethoxysilyl)propyl]octadecyldimethylammonium chloride (TPOAC) as the mesoporous template and sole silica source, together with tetraethylammonium hydroxide (TEAOH) as the microporous director.[31] Still, the obtained material had much weaker acidity than conventional SAPO-34 molecular sieves. Although abundant mesopores are obtained, the application of SAPO-34 as a catalyst is limited. Very recently, Yu *et al.* reported success in the preparation of hierarchical SAPO-34 with enhanced MTO catalytic performance also by using TPOAC as the mesoporous director and morpholine (MOR) as the microporous template.[32] The disparate results from the same mesoporogen TPOAC suggest that the microporous template may also play a crucial role in the synthesis of hierarchical SAPO-34. In addition, the role of TPOAC as a silica source during the crystallization process still deserves investigation.

In this work, exploration on the synthesis of hierarchical SAPO-34 was continued by using TPOAC as the mesoporogen and diethylamine (DEA) as the microporous template. Sphere-like SAPO-34 molecular sieves consisting of interpenetrating nanosheets were synthesized and well characterized. The influence of various synthetic parameters, roles of the dual templates as well as the catalytic properties of SAPO-34s were investigated in detail. The deactivation behavior of the hierarchical SAPO-34 catalyst was studied and discussed.

2 Experimental

2.1 Synthesis

Orthophosphoric acid (H_3PO_4, 85 wt%), tetraethyl orthosilicate (TEOS, 98 wt%), aluminium isopropoxide ($Al(i\text{-}C_3H_7O)_3$, 99 wt%) and diethylamine (DEA, 99 wt%) were purchased from Tianjin Kemiou Chemical Reagent Company. Silica sol (30.1 wt%) was purchased from Shenyang Chemical Company, and pseudoboehmite (72.5 wt%) was purchased from Fushun Petroleum No. 3 Factory. [3-(Trimethoxysilyl)propyl]octadecyldimethylammonium chloride ($[[(CH_3O)_3SiC_3H_6N(CH_3)_2\text{-}C_{18}H_{37}]Cl$, TPOAC, 65 wt%) was purchased from Aladdin Chemical Incorporation. All chemicals were used as received without further purification.

A certain amount of TPOAC was firstly added into deionized water and stirred overnight. Then, the desired amounts of $Al(i\text{-}C_3H_7O)_3$, DEA, TEOS and H_3PO_4 were added in sequence. After further stirring for 2–5 h, the obtained gels with a molar composition of (2.0–2.5) DEA : $1.0Al_2O_3$: $1.0P_2O_5$: (0.4–0.6) SiO_2 : $150H_2O$ were transferred into stainless steel autoclaves, and heated at 200 °C for 72 h statically under autogenous pressure. The products were filtered, washed thoroughly and dried in air. Then the samples were calcined at 600 °C for 2 h to remove the template if necessary. For comparison, conventional SAPO-34 with a similar silica content was prepared by using the same template DEA. The detailed synthesis and characterization information are provided in the ESI.†

The yields of products were calculated using the following equation: yield $= (M_{sample} \times 75\%)/M_{(Al_2O_3 + P_2O_5 + SiO_2)_{gel}} \times 100\%$, where M_{sample} and $M_{(Al_2O_3 + P_2O_5 + SiO_2)_{gel}}$ stand for the weights of the products and the dry mass of inorganic oxides in the starting mixture respectively. 75% is the estimated average value of framework compounds included in the samples.

2.2 Characterization

The powder XRD pattern was recorded on a PANalytical X' Pert PRO X-ray diffractometer with Cu-Kα radiation ($\lambda = 1.54059$ Å), operating at 40 kV and 40 mA. The chemical composition of the samples was determined with a Philips Magix-601 X-ray fluorescence (XRF) spectrometer. The crystal morphology was observed by scanning electron microscopy (SEM) using a TM3000 (Hitachi) and field emission SEM (Hitachi SU8020). Transmission electron microscopy (TEM) images and selected area electron diffraction (SAED) patterns were recorded with a JEM-2100 electron microscope. Textural properties of the calcined samples were determined by N_2 adsorption–desorption at 77 K on a Micromeritics ASAP 2020 system. The total surface area was calculated based on the BET equation. The micropore volume and micropore surface area were evaluated using the *t*-plot method. Mesopore volume and mesopore surface area were evaluated from the adsorption isotherm by the Barrett–Joyner–Halenda (BJH) method. The temperature-programmed desorption of ammonia (NH_3-TPD) was carried out with an AutochemII2920 equipment (Micromeritics). 0.2 grams of the sample particles (40–60 mesh) were loaded into a U-quartz tube and pretreated at 650 °C for 60 min under He flow. After cooling down to 100 °C, a gas mixture of NH_3 and He flow was introduced to saturate the sample surface with NH_3 adsorption (60 min). After this, He flow was purged through the sample for 30 min to remove the weakly adsorbed NH_3 molecules. The measurement of the desorbed NH_3 was performed from 100 °C to 650 °C (10 °C min^{-1}) under He flow (20 ml min^{-1}). ^{13}C magic-angle-spinning (MAS) nuclear magnetic resonance (NMR), ^{29}Si cross-polarization (CP)/MAS NMR and ^{1}H MAS NMR analyses were carried out on a Bruker AvanceIII 600 spectrometer at 150.9 MHz for ^{13}C, 119.2 MHz for ^{29}Si and 600.13 MHz for ^{1}H. ^{29}Si CP/MAS NMR spectra were measured with a contact time of 3 ms and a recycle delay of 2 s. ^{29}Si CP/MAS NMR spectra were recorded with a 4 mm MAS probe with a spinning rate of 8 kHz. ^{13}C MAS NMR spectra and ^{1}H MAS NMR spectra were recorded with a 4 mm MAS probe at a spinning rate of 12 kHz. Chemical shifts were referenced to 4,4-dimethyl-4-silapentane sulfonate sodium salt (DSS) for ^{29}Si, and adamantane for ^{13}C and ^{1}H. Thermogravimetric and differential thermal analysis (TG and DTA) were performed on a TA SDTQ600 analyzer with a temperature-programmed rate of 10 °C min^{-1} in air. The ammonia-adsorbed infrared (NH_3-adsorbed IR) and pyridine-adsorbed IR spectra were carried out on a Bruker Tensor 27 instrument. The calcined samples were dehydrated at 500 °C for 1 h under a vacuum of 1.0×10^{-2} Pa, and then pure ammonia or pyridine vapor was adsorbed at room temperature for 10 min. After reaching equilibrium, the ammonia-adsorbed system was evacuated at 200 °C, 300 °C and

400 °C, and the pyridine-adsorbed system was evacuated at 100 °C and 300 °C. The IR spectra were recorded at the corresponding temperatures, respectively.

2.3 Catalytic test and retained coke analysis

The methanol to olefins (MTO) reaction was performed in a quartz tubular fixed-bed reactor at atmospheric pressure. 0.3 g calcined catalyst (40–60 mesh) was loaded in the quartz reactor and activated at 550 °C in a He flow of 30 ml min^{-1} for 1 h before starting each reaction run, and then the temperature was adjusted to a reaction temperature of 450 °C. Methanol was fed by passing the carrier gas (42 ml min^{-1}) through a saturator containing methanol at 30 °C, which gave a weight hourly space velocity (WHSV) of 3 h^{-1}. The reaction products were analyzed using an online gas chromatograph (Agilent GC 7890N), equipped with a flame ionization detector (FID) and Plot-Q column.

The retained organics in the deactivated SAPO-34 catalysts after the MTO reaction were analyzed according to the procedure introduced by Guisnet.[33] The completely deactivated catalysts were first dissolved with a HF solution (20 wt%), and then the organic compounds present in them were extracted by using CH_2Cl_2 and analyzed by a gas chromatograph equipped with a FID detector and a mass sensitive detector (Agilent 7890A/5975C) using a capillary column of HP-5.

3 Results and discussion

3.1 Synthesis and characterizations

The synthesis conditions of hierarchical SAPO-34 and the corresponding results are listed in Table 1. The selected XRD patterns are shown in Fig. 1. A pure SAPO-34 phase can be prepared when the molar ratio of SiO_2/Al_2O_3 is higher than 0.4, and the DEA/Al_2O_3 ratio is above 2.0. The yields are around 42%, which are slightly lower than that of SAPO-34 synthesized without TPOAC (48.2%, sample 5) due to the introduction of the mesoporogen. It is noted that a lower SiO_2/Al_2O_3 ratio and insufficient DEA result in impurities such as SAPO-11 (sample 1) and SAPO-5 (sample 2), respectively. Even under optimized conditions, DNL-6 appears as a metastable phase during the crystallization process, which disappears after a considerable reaction time (Fig. S3 and S4†). In addition, the addition of TPOAC slows down the crystallization rate significantly, while it takes at least 72 hours in order to obtain a SAPO-34 phase with satisfactory crystallinity. Comparatively, well-crystallized SAPO-34 with a minor DNL-6 impurity could be obtained in 24 h under the same conditions but without TPOAC (sample 5, Fig. S5†). Keeping the SiO_2/Al_2O_3 ratio of the gel at 0.5, the molar ratio of TPOAC/TEOS was adjusted from 1/9 to ∞. All synthesized samples exhibit the typical XRD peaks of SAPO-34 with high intensity except sample 9. Sample 9 is synthesized by using TPOAC as the only silica source, which leads to SAPO-5 with low crystallinity. More interestingly, samples 6–8 have an obviously increased silica content due to the higher TPOAC/TEOS molar ratio. It is deduced that the interaction between TPOAC and TEOS may enhance the activity of the silica source which promotes the introduction of silica atoms into the framework. When TEOS is absent, the activity of TPOAC is low, and only a small amount of the Si source is involved in the reaction which leads to the SAPO-5 phase.

The morphologies of the SAPO-34 products change much with the increased molar ratio of TPOAC/TEOS. As seen in Fig. 2, sample 6 presents as spherical agglomerates composed of many micrometer-sized cubic crystals, while sample 7 evolves into a self-assembly of spherical nanosheets as the TPOAC/TEOS ratio

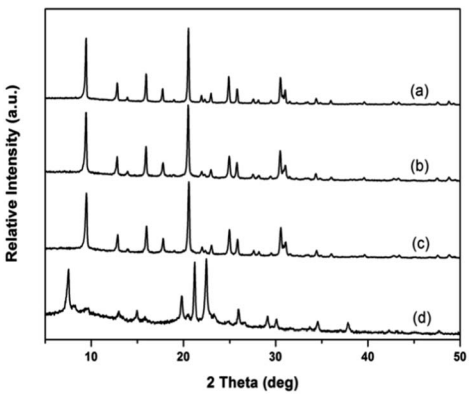

Fig. 1 XRD patterns of as-synthesized samples 6 (a), 7 (b), 8 (c) and 9 (d).

Table 1 Synthesis conditions,[a] yields and composition of products analyzed by XRF

Sample	x	y	TPOAC/TEOS	Product	Product yield	Product composition
1	0.4	2.3	1/3	SAPO-34 + SAPO-11	42.3%	—
2	0.5	2.0	1/3	SAPO-34 + SAPO-5	43.3%	—
3	0.5	2.5	1/3	SAPO-34	43.6%	$Al_{0.486}P_{0.361}Si_{0.153}O_2$
4	0.6	2.3	1/3	SAPO-34	45.5%	$Al_{0.467}P_{0.367}Si_{0.166}O_2$
5[b]	0.5	2.3	0	SAPO-34 + DNL-6	48.2%	—
6	0.5	2.3	1/9	SAPO-34	42.1%	$Al_{0.483}P_{0.358}Si_{0.141}O_2$
7	0.5	2.3	1/3	SAPO-34	41.5%	$Al_{0.491}P_{0.360}Si_{0.149}O_2$
8	0.5	2.3	1/1	SAPO-34	39.4%	$Al_{0.493}P_{0.366}Si_{0.159}O_2$
9	0.5	2.3	∞	SAPO-5 + amorphous	—	—

[a] The initial gel molar composition: $Al_2O_3/P_2O_5/SiO_2/DEA/H_2O = 1.0/1.0/x/y/150$, crystallization conditions: 200 °C, 72 h. [b] The crystallization time is 24 h, and the estimated value of framework compounds is 85% used for the yield calculation.

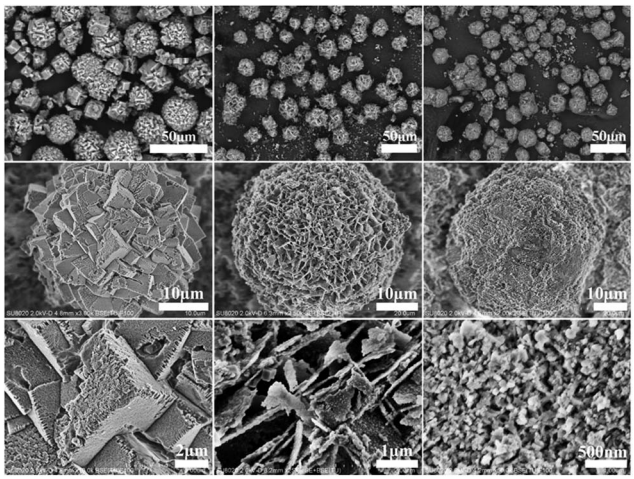

Fig. 2 SEM images of calcined samples 6 (left), 7 (middle) and 8 (right).

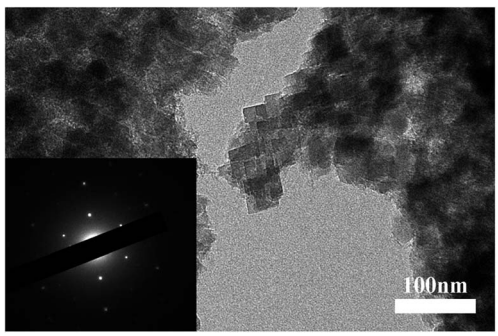

Fig. 3 TEM image and SAED pattern (inset) of the calcined sample 7.

increases from 1/9 to 1/3. The thickness of each nanosheet is around 50 nm. When the TPOAC/TEOS ratio reaches 1/1 (sample 8), the nanosheets disappear. Instead, SAPO-34 with an elliptical morphology appears which consists of aggregates of *ca.* 50 nm particles. TEM was used to investigate the details of the structural features of nanosheets belonging to sample 7. Fig. 3 reveals that the nanosheets are spliced together by countless nano-square pieces. Mesopores can be observed within the nanosheets. Selected area electron diffraction (SAED) further confirms the crystallinity of the nanosheets (Fig. 3, inset). The distinct diffraction pattern can be indexed according

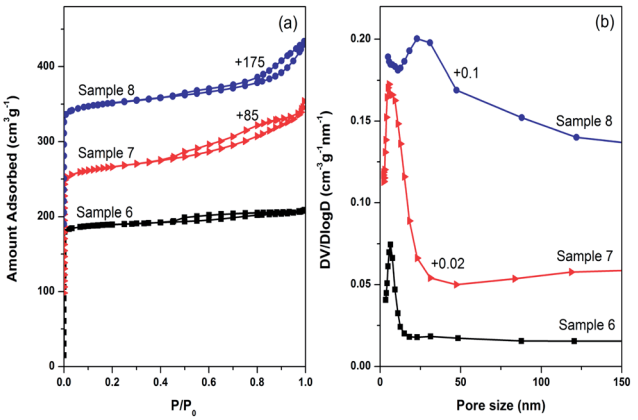

Fig. 4 Nitrogen adsorption–desorption isotherms (a) and BJH pore size distributions (b) of samples 6, 7 and 8.

to the CHA type zeolite structure in the [001] direction, which demonstrates that the nano-square crystals have a consistent growth orientation and arrangement. It is deduced that the crystals of sample 7 grow preferentially along the plane corresponding to the {001} crystal plane group.

The textural properties of samples 6–8 were characterized by N_2 adsorption–desorption experiments. As illustrated in Fig. 4a, all the three adsorption–desorption isotherms have steep uptakes near $P/P_0 = 0$ due to the microporous structure. Remarkable differences among the three isotherms lie in the region of $P/P_0 > 0.4$. A very small hysteresis loop exists in the region $0.45 < P/P_0 < 0.7$ for sample 6, while there are manifest hysteresis loops at $P/P_0 = 0.45$–0.9 for sample 7, and at $P/P_0 =$ 0.7–0.9 for sample 8. The increased adsorption quantity at the medium-pressure region is interpreted as capillary condensation in the mesopores. The abrupt inclination at a relatively high pressure of $P/P_0 > 0.9$ is associated with multilayer adsorption between the intercrystal pores of nanoparticles. The mesopore size distribution for samples 6 and 7 is 3–15 nm and 3–30 nm, respectively (Fig. 4b). The latter consists of richer mesopores which is reflected in the higher distribution peak. Sample 8 has a wider pore distribution with the maximum at 25 nm. Based on the above analyses, it is believed that sample 7 has the most abundant mesopores with a relatively narrow distribution among the three samples. Their textural properties, summarized in Table 2, further confirm our conclusions. All the

Table 2 Textural properties and the acid amount of the samples

	Textural properties					Acid amount[f] (mmol g^{-1})		
Sample	S_{BET}[a] (m^2 g^{-1})	S_{mic}[b] (m^2 g^{-1})	S_{Ext}[c] (m^2 g^{-1})	V_{mic}[d] (cm^3 g^{-1})	V_{meso}[e] (cm^3 g^{-1})	Weak	Medium and strong	Total
6	631	584	47	0.27	0.05	1.48	1.42	2.90
7	591	484	107	0.23	0.18	1.37	1.38	2.75
8	565	464	101	0.21	0.17	0.50	0.54	1.04
Conventional SAPO-34	588	586	2	0.28	0	1.68	1.93	3.61

[a] BET surface area. [b] *t*-Plot micropore surface area. [c] *t*-Plot external surface area. [d] *t*-Plot micropore volume. [e] BJH adsorption volume. [f] Calculated from the peak area of NH_3-TPD profiles.

three samples have a high BET surface area above 560 $m^2\ g^{-1}$ and a large micropore volume of 0.20–0.27 $cm^3\ g^{-1}$, confirming the high crystallinity of these samples. In addition, sample 7 has the largest external surface area of 107 $m^2\ g^{-1}$ and mesopore volume of 0.18 $cm^3\ g^{-1}$.

The acidic properties of samples 6, 7 and 8 were investigated by NH_3-TPD measurements by comparing with those of conventional SAPO-34. As seen in Fig. 5, there are two desorption peaks at about 180–200 °C and 400–470 °C for all samples, which correspond to weak and strong acid sites, respectively. The amounts of acid sites were roughly determined through the NH_3-TPD profiles, and are listed in Table 2. The large amount of acid sites is consistent with the high Si contents of the products synthesized with the DEA template. It is clear that samples 6, 7 and 8 prepared with TPOAC show lower desorption temperature and smaller acid amount than the conventional SAPO-34. Comparing samples 6, 7 and 8, the acidity decreases with increase in the TPOAC/TEOS ratio in the initial gel. Obviously, sample 8 possesses much weaker acid strength and much smaller acid amount than the other two samples. These results suggest that the introduction of TPOAC can weaken the acidity of SAPO-34. The strength and type of acid sites were further characterized by IR spectroscopic studies of ammonia and pyridine sorption at varied temperatures. The NH_3-adsorbed IR spectra of samples 6–8 and conventional SAPO-34 at various temperatures are shown in Fig. S6.† For NH_3-adsorbed IR spectra, the bands at 1456 and 1619 cm^{-1} can be assigned to the δ_{asym} of NH_3 bonded to Brønsted and Lewis acid sites, respectively.[34,35] The strength of acid sites can be distinguished from the differences of IR spectra obtained at different temperatures. As shown in Fig. S6,† the IR signals attributed to the adsorbed NH_3 disappeared at 300 °C and 400 °C for samples 8 and 7 respectively, while minor signals were still detected for sample 6 and conventional SAPO-34 at 400 °C. It is believed that the strength of acid sites decreases in the order of conventional SAPO-34/sample 6 > sample 7 > sample 8, which is consistent with the result obtained from the NH_3-TPD measurements. The acidity of the external surface was also detected through the pyridine-adsorbed IR spectra (Fig. S7†) because the bigger pyridine (kinetic diameter: 0.57 nm) cannot enter the channels of SAPO-34 (0.38 nm). This shows that samples 7 and 8 have stronger Brønsted and Lewis acid sites on the external surface due to their larger external surface.

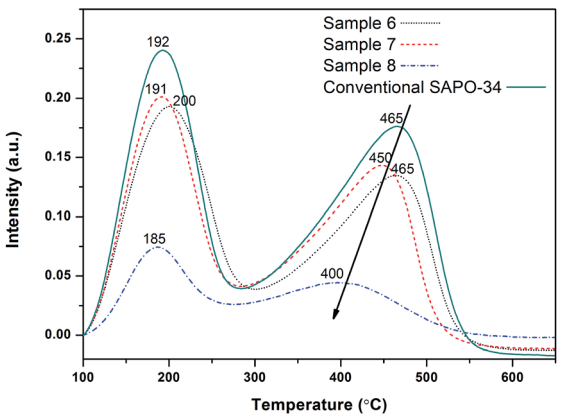

Fig. 5 NH_3-TPD profiles of samples 6, 7, 8 and conventional SAPO-34.

3.2 Effect of TPOAC

The above characterizations clearly demonstrate that the introduction of TPOAC has a significant impact on the crystallization of SAPO-34. In order to investigate the role of TPOAC, sample 7 was selected to measure the ^{13}C and ^{29}Si NMR. The ^{13}C MAS NMR spectrum is illustrated in Fig. 6a. Two peaks at 42 (A) and 10.7 ppm (B) corresponding to DEA can be easily identified on the basis of our previous report.[36] The strongest signal at 30.8 ppm (g) is attributed to methylene moieties belonging to the long-alkyl chain of TPOAC. All the other peaks can also be ascribed to the corresponding groups of TPOAC which proves its presence.[37,38] The signal at 59.3 ppm ascribed to Si–OCH_3 is negligible, which indicates that Si–OCH_3 is hydrolyzed mostly during the reaction. The ^{29}Si CP NMR spectrum of the as-synthesized sample 7 and MAS NMR spectrum for the calcined sample 7 are shown in Fig. 6b. Both ^{29}Si spectra give a clear resonance signal at −89 ppm due to $Si(OAl)_4$ species.[39] A broad signal at −55 to −75 ppm is detected for the as-synthesized sample, which is attributed to the T_n groups (T_n = $RSi(OAl)_n(OH)_{3-n}$, n = 2 and 3).[40,41] It indicates that the organo-siloxanes are connected to the silicoaluminophosphate framework. After calcination, the resonance signal at −55 to −75 ppm disappears, and two new shoulder peaks at about −80 and −85 ppm arise instead. It may be caused by the breaking of

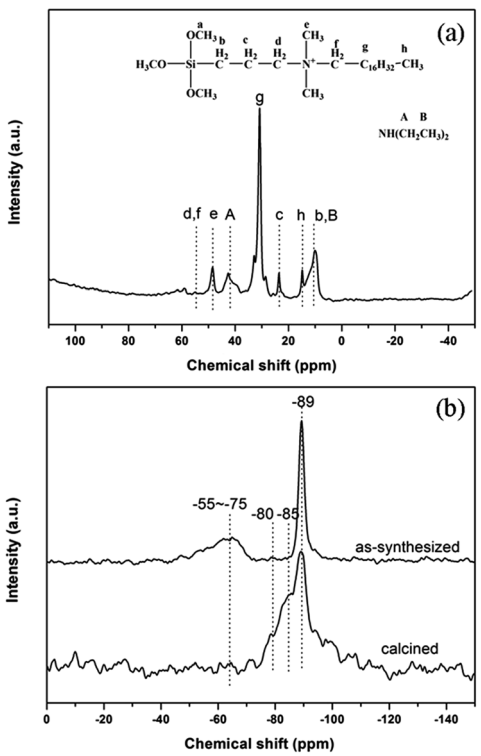

Fig. 6 ^{13}C MAS NMR spectrum of as-synthesized sample 7 (a), ^{29}Si CP NMR spectrum of as-synthesized sample 7 and MAS NMR spectrum of calcined sample 7 (b).

Si–C bonds due to the removal of organic groups, where $Si(OAl)_3OH$ and $Si(OAl)_2(OH)_2$ species are formed as the defect sites afterwards.[41] The appearance of the Si–OH group is also confirmed by ^1H MAS NMR spectroscopy (Fig. S8†).

TG and DTA analyses were performed to examine the organics of the samples. As seen in Fig. 7, conventional SAPO-34 has only one obvious exothermic peak at 435 °C in the DTA curve corresponding to the DEA loss of *ca.* 14.6 wt% from 380 °C to 650 °C in the TG curve. The SAPO-34s prepared with TPOAC exhibit broader exothermic signals before 435 °C in their DTA curves, and the weight losses occur smoothly after 200 °C. The total weight losses are 17.5, 21.6 and 25.7 wt% for samples 6, 7 and 8, respectively. The additional exothermic peaks and weight losses are ascribed to the combustion of TPOAC. Although the precise amount of TPOAC cannot be determined, it is certain that the introduced amount of TPOAC increases with increase in the TPOAC/TEOS ratio.

Surfactants have been widely used to control the morphology of well-structured materials due to their efficient self-assembly properties.[29,42–44] Schwieger *et al.* synthesized house-of-cards-like mesoporous zeolite X by using the organosilane surfactant 3-(trimethoxysilyl)propyl hexadecyl dimethylammonium chloride (TPHAC).[29] They believed that the interplay between the surface activity of the $TPHA^+$ molecules and the charge-balancing effects of the inorganic cations leads to the formation of micellar assemblies and directs the formation of the special zeolite morphology. Fan *et al.* synthesized different sized SAPO-11 with cationic surfactants.[43] They proved the adsorption behavior of the surfactant on the SAPO precursor through zeta potential measurements at different crystallization times of SAPO-11. In our work, the product morphology changes obviously with the increased amount of TPOAC (Fig. 2). Besides, the time-consuming experiments present an intergrowing morphology in a 12 hour reaction (Fig. S3a and S4a†). It suggests that the interplay between the surfactants and the SAPO precursors happens from the beginning of the reaction. Referring to the investigation results by Zhang *et al.*,[44] the surfactant may act as a crystal face inhibitor preferentially absorbed onto certain specific planes. The anisotropic growth of the crystal is therefore triggered. Moreover, the surfactant may be a very potent surface stabilizer, which could lower the energy cost for creating new surfaces, thus affecting crystal splitting and prompting the formation of hierarchical architectures from individual crystals. A possible crystallization process is therefore proposed and illustrated in Scheme 1. SAPO precursors with adsorbed cationic surfactants are firstly formed. If a small amount of TPOAC is involved, the crystal growth of SAPO-34 is not obstructed so much by the surfactants, and the rhombohedral crystals still form, but with a certain degree of twinning. When the concentration of TPOAC is in a suitable range, the self-assembly of TPOAC directs the formation of the intergrowth of SAPO-34 nanosheets. However, if the

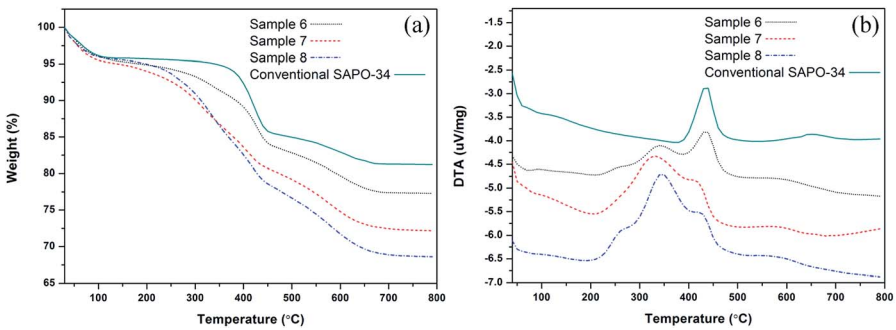

Fig. 7 TG (a) and DTA (b) curves of samples 6, 7, 8 and conventional SAPO-34.

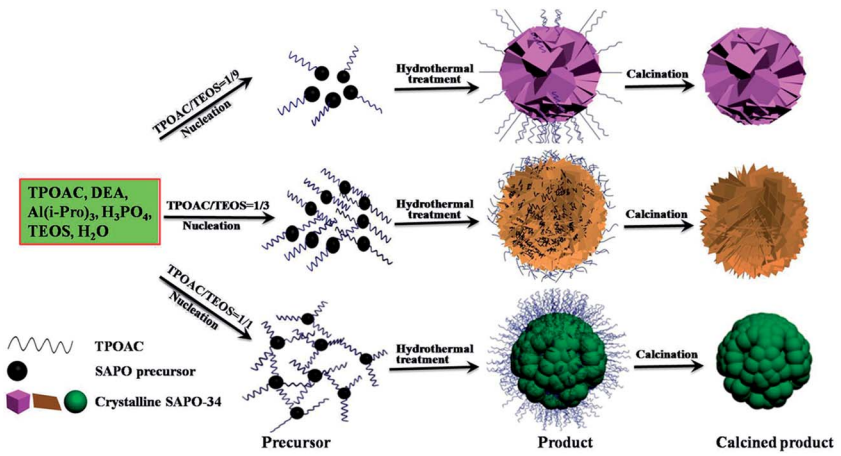

Scheme 1 The proposed crystallization process of SAPO-34s with different TPOAC/TEOS ratios.

amount of TPOAC is very high, the inhibition of crystal growth is so serious that only nanoparticles are formed. Mesoporosity is generated when TPOAC is removed by calcination. Notably, the loss of mesoporosity for sample 8 might be more because the nanoparticles accumulate randomly and gather more closely after the removal of TPOAC. So the external surface and mesopore volume are comparable for samples 7 and 8 even if the content of TPOAC is higher for sample 8.

3.3 Role of the microporous template

Compared to the reported hierarchical SAPO-34 directed by TEAOH[31] and MOR,[32] SAPO-34 synthesized herein using DEA has distinct morphology and acidic property. The result demonstrates again that the microporous template plays an important role in the synthesis of mesoporous SAPO-34. Generally, TEAOH tends to direct SAPO-34 crystallites, while DEA and MOR lead to micrometer-sized SAPO-34 crystals. The latter two templates tend to introduce more silica atoms into the framework which results in more acidic sites.[45] Considering that the introduction of TPOAC can weaken the acidity of SAPO molecular sieves, it is supposed that the template leading to silica-rich SAPO-34 is more suitable for the synthesis of mesoporous SAPO-34 together with TPOAC. Otherwise, the desired acidity of conventional SAPO-34 bestowed by a microporous template, such as TEAOH, might be further weakened.

3.4 Catalytic test

The catalytic properties of the samples were evaluated using the MTO reaction in a fixed-bed reactor, and the results are given in Fig. 8 and Table 3. Sample 6 exhibits the shortest catalytic lifetime of 72 min and 77.97% selectivity for ethylene and propylene, which are even worse than those of conventional SAPO-34 with a similar silica content and the same structure directing agent DEA. The reason could be the bigger bulk crystal size of *ca.* 30 μm for sample 6 which leads to a longer diffusion path and accelerates coke deposition.[46] Thankfully, the catalytic performance of sample 7 has been remarkably improved. The methanol conversion over 99% could be retained for 308 min, which is much longer than that of conventional SAPO-34 (157 min). The selectivity for ethylene and propylene is comparable to that of conventional SAPO-34 (81.16 *vs.* 81.99%). The generated mesopores and the small crystal size of sample 7 shorten the diffusion paths, which greatly enhance the mass transfer during methanol conversion. The satisfactory selectivity to light olefins could be attributed to the retention of its excellent microporosity. Notably, sample 8 has a declining lifetime (226 *vs.* 308 min) and selectivity to light olefins (78.94 *vs.* 81.16%) in comparison with sample 7 although they have comparable mesoporosity. A possible reason is that sample 8 possesses much weaker acid strength and lower acid amount as shown in NH_3-TPD profiles (Fig. 5). Normally, SAPO-34 with lower acid strength and acidic amount exhibits slower catalyst deactivation and better MTO catalytic performance. However, a catalyst with the fewest acid sites does not necessarily have the longest lifetime.[12] The available acid sites may be gradually covered by coke, resulting in faster deactivation. Therefore, in order to achieve optimal catalytic performance for the SAPO-34 catalyst, it is sensible to balance both mesoporosity and microporosity, and control the acidity precisely. Catalyst regeneration experiments were performed for sample 7 by calcination at 600 °C for 2 h. And then, the MTO reaction was repeated under the same conditions. The recycled catalyst showed a slightly longer lifetime (342 *vs.* 308 min) and lower selectivity to light olefins (80.89 *vs.* 81.16%). The result confirms the excellent stability of the hierarchical SAPO-34. The changes in lifetime and selectivity may be the result of the change in acidity during calcination.[47]

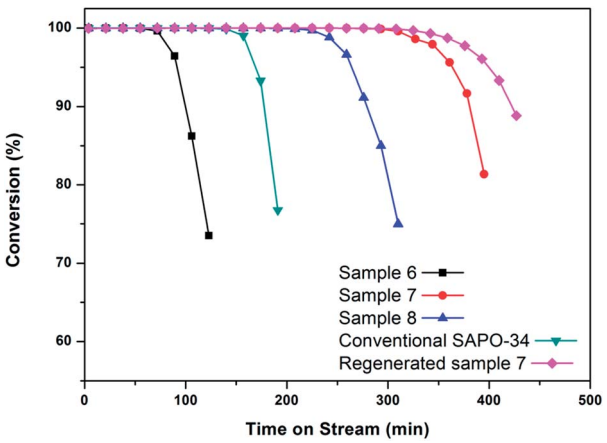

Fig. 8 Methanol conversion variation with time-on-stream over samples 6, 7, 8, conventional SAPO-34 and regenerated sample 7. Experimental conditions: WHSV = 3 h^{-1}, T = 450 °C, catalyst weight = 300 mg.

Table 3 Lifetime[a] and product distribution[b] of SAPO-34s in the MTO reaction (WHSV = 3 h^{-1}, T = 450 °C)

Sample	Lifetime (min)	$C_2^=$ (%)	$C_3^=$ (%)	$C_2^= + C_3^=$ (%)	C_3H_8 (%)	C_4–C_6 (%)	Coke content[c] (%, g g_{cat}^{-1})	R_{coke}[c] (mg min^{-1})
6	72	42.32	35.65	77.97	4.66	12.73	—	—
7	308	49.71	31.44	81.16	0.73	13.99	19.65	0.214
7[d]	342	48.41	32.48	80.89	2.72	12.99	—	—
8	226	48.19	30.74	78.94	0.88	16.43	—	—
Conventional SAPO-34	157	47.56	34.43	81.99	3.58	12.31	14.91	0.335

[a] Catalyst lifetime is defined as the reaction duration with >99% methanol conversion. [b] Based on the highest selectivity of ethene and propene under >99% methanol conversion. [c] Determined using a TG and DTA analyzer up to 800 °C measured after the MTO reaction; R_{coke} = coke amount/reaction time. [d] After deactivation, sample 7 was recycled after regeneration.

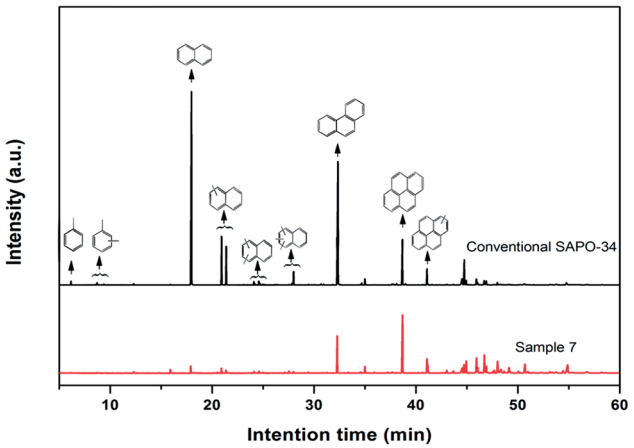

Fig. 9 GC-MS chromatograms of occluded organic species retained in sample 7 and conventional SAPO-34 after the MTO reaction. The structures annotated on the chromatograms are peak identifications in comparison with the mass spectra of those in the NIST database.

In order to understand well the deactivation process of the hierarchical SAPO-34 catalyst, the amount of deposited coke and species of deactivated sample 7 and conventional SAPO-34 catalysts were analyzed after the MTO reaction. The weight losses of sample 7 and conventional SAPO-34 are 19.65% and 14.91%, respectively (Table 3), which are due to the combustion of the retained coke species. Considering that coke was deposited for different reaction times for the two catalysts (481 min for sample 7 and 208 min for conventional SAPO-34), the average coke formation rate was calculated using the following equation: R_{coke} = coke amount/reaction time. Coke formation rate of sample 7 (0.214) is much slower than that of conventional SAPO-34 (0.335) which agrees with the lower hydrogen transfer index (C_3H_8/C_3H_6, Fig. S9†) and longer lifetime of sample 7. The GC-MS chromatograms corresponding to various deposited coke species of the two catalysts are shown in Fig. 9. It is obvious that naphthalene, phenanthrene and pyrene are the main coke species of conventional SAPO-34. However, the peak intensity of naphthalene and naphthalene derivatives are found to be weaker for sample 7. Normally, it is believed that naphthalene and its derivatives can get converted to heavier constituents such as phenanthrene and pyrene when they have access to light molecules together with catalytic centers.[48,49] Thus, the smaller amounts of residues of naphthalene and its derivatives of sample 7 should be ascribed to the introduced mesopores which provide larger space for diffusion and make the further reaction for naphthalene and its derivatives happen. The peaks with a retention time of above 45 min should be attributed to polycyclic aromatics with more than four fused rings. These retained compounds are too big to be accommodated in the CHA cage of SAPO-34 and hence form on the external surface of the catalysts.[16] The richer external surface of sample 7 leads to relatively more pyrene and bigger polycyclic aromatics.

4 Conclusion

By using the quaternary ammonium-type organosilane surfactant TPOAC and microporous template DEA, highly crystallized hierarchical SAPO-34 molecular sieves have been hydrothermally synthesized in one step with improved catalytic stability for the MTO process. ^{13}C and ^{29}Si NMR clearly prove the existence of TPOAC in the products which indicates that it is involved in the formation of SAPO-34 as a mesoporogen and a part of silica source. The morphology and acidity of SAPO-34 are therefore optimized which contribute to enhance its catalytic ability. This work demonstrates that the soft-template method is feasible for the synthesis of hierarchical SAPO-34. In the meantime, the microporous template, responsible for retaining the inherent microporosity and acidity of silicoaluminophosphate molecular sieves, should be paid sufficient attention. More highly effective hierarchical SAPO catalysts are expected to be prepared with the understanding of the crystallization process and the roles of mesoporous and microporous templates.

Acknowledgements

We are thankful for the financial support from the National Natural Science Foundation of China (21476228 and 21101150).

Notes and references

1 B. M. Lok, C. A. Messina, R. L. Patton, R. T. Gajek, T. R. Cannan and E. M. Flanigen, *J. Am. Chem. Soc.*, 1984, **106**, 6092–6093.
2 B. M. Lok, C. A. Messina, R. L. Patton, R. T. Gajek, T. R. Cannan and E. M. Flanigen, *US Pat.* 4440871, 1984.
3 R. L. Bedard, in *Zeolites in Industrial Separation and Catalysis*, ed. S. Kulprathipanja, Wiley-VCH, Weinheim, Germany, 2010, pp. 61–84.
4 S. T. Wilson, *Stud. Surf. Sci. Catal.*, 2007, **168**, 105–135.
5 H. O. Pastore, S. Coluccia and L. Marchese, *Annu. Rev. Mater. Res.*, 2005, **35**, 351–395.
6 Z. M. Liu and J. Liang, *Curr. Opin. Solid State Mater. Sci.*, 1999, **4**, 80–84.
7 J. M. Campelo, F. Lafont and J. M. Marinas, *J. Catal.*, 1995, **156**, 11–18.
8 S. G. Li, J. L. Falconer and R. D. Noble, *Adv. Mater.*, 2006, **18**, 2601–2603.
9 X. Su, P. Tian, D. Fan, Q. H. Xia, Y. Yang, S. T. Xu, L. Zhang, Y. Zhang, D. H. Wang and Z. M. Liu, *ChemSusChem*, 2013, **6**, 911–918.
10 J. Liang, H. Y. Li, S. Zhao, W. G. Guo, R. H. Wang and M. L. Ying, *Appl. Catal.*, 1990, **64**, 31–40.
11 A. J. Marchi and G. F. Froment, *Appl. Catal.*, 1991, **71**, 139–152.
12 S. Wilson and P. Barger, *Microporous Mesoporous Mater.*, 1999, **29**, 117–126.
13 L. Xu, A. P. Du, Y. X. Wei, S. H. Meng, Y. L. He, Y. L. Wang, Z. X. Yu, X. Z. Zhang and Z. M. Liu, *Chin. J. Catal.*, 2008, **29**, 727–732.

14 J. Zhu, Y. Cui, Y. Wang and F. Wei, *Chem. Commun.*, 2009, 3282–3284.
15 D. Fan, P. Tian, X. Su, Y. Y. Yuan, D. H. Wang, C. Wang, M. Yang, L. Y. Wang, S. T. Xu and Z. M. Liu, *J. Mater. Chem. A*, 2013, **1**, 14206–14213.
16 G. J. Yang, Y. X. Wei, S. T. Xu, J. R. Chen, J. Z. Li, Z. M. Li, J. H. Yu and R. R. Xu, *J. Phys. Chem. C*, 2013, **117**, 8214–8222.
17 M. Yang, P. Tian, C. Wang, Y. Y. Yuan, Y. Yang, S. T. Xu, Y. L. He and Z. M. Liu, *Chem. Commun.*, 2014, **50**, 1845–1847.
18 H. Q. Yang, Z. C. Liu, H. X. Gao and Z. K. Xie, *J. Mater. Chem.*, 2010, **20**, 3227–3231.
19 F. Schmidt, S. Paasch, E. Brunner and S. Kaskel, *Microporous Mesoporous Mater.*, 2012, **164**, 214–221.
20 D. Y. Xi, Q. M. Sun, J. Xu, M. Cho, H. S. Cho, S. Asahina, Y. Li, F. Deng, O. Terasaki and J. H. Yu, *J. Mater. Chem. A*, 2014, **2**, 17994–18004.
21 M. Choi, H. S. Cho, R. Srivastava, C. Venkatesan, D. H. Choi and R. Ryoo, *Nat. Mater.*, 2006, **5**, 718–723.
22 F. S. Xiao, L. F. Wang, C. Y. Yin, K. F. Lin, Y. Di, J. X. Li, R. R. Xu, D. S. Su, R. Schlogl, T. Yokoi and T. Tatsumi, *Angew. Chem., Int. Ed.*, 2006, **45**, 3090–3093.
23 M. Choi, K. Na, J. Kim, Y. Sakamoto, O. Terasaki and R. Ryoo, *Nature*, 2009, **461**, 246–249.
24 K. Na, C. Jo, J. Kim, K. Cho, J. Jung, Y. Seo, R. J. Messinger, B. F. Chmelka and R. Ryoo, *Science*, 2011, **333**, 328–332.
25 J. Zhu, Y. H. Zhu, L. K. Zhu, M. Rigutto, A. van der Made, C. G. Yang, S. X. Pan, L. Wang, L. F. Zhu, Y. Y. Jin, Q. Sun, Q. M. Wu, X. J. Meng, D. L. Zhang, Y. Han, J. X. Li, Y. Y. Chu, A. M. Zheng, S. L. Qiu, X. M. Zheng and F. S. Xiao, *J. Am. Chem. Soc.*, 2014, **136**, 2503–2510.
26 Y. Cui, Q. Zhang, J. He, Y. Wang and F. Wei, *Particuology*, 2013, **11**, 468–474.
27 F. Wang, L. Sun, C. L. Chen, Z. Chen, Z. W. Zhang, G. H. Wei and X. M. Jiang, *RSC Adv.*, 2014, **4**, 46093–46096.
28 K. Cho, H. S. Cho, L. C. de Menorval and R. Ryoo, *Chem. Mater.*, 2009, **21**, 5664–5673.
29 A. Inayat, I. Knoke, E. Spiecker and W. Schwieger, *Angew. Chem., Int. Ed.*, 2012, **51**, 1962–1965.
30 M. Choi, R. Srivastava and R. Ryoo, *Chem. Commun.*, 2006, 4380–4382.
31 L. Chen, R. W. Wang, S. Ding, B. B. Liu, H. Xia, Z. T. Zhang and S. L. Qiu, *Chem. J. Chin. Univ.*, 2010, **9**, 1693–1696.
32 Q. M. Sun, N. Wang, D. Y. Xi, M. Yang and J. H. Yu, *Chem. Commun.*, 2014, **50**, 6502–6505.
33 M. Guisnet, *J. Mol. Catal. A: Chem.*, 2002, **182**, 367–382.
34 Z. M. Wang, Z. J. Tian, F. Teng, G. D. Wen, Y. P. Xu, Z. S. Xu and L. W. Lin, *Catal. Lett.*, 2005, **103**, 109–116.
35 J. Datka, B. Gil and A. Kubacka, *Zeolites*, 1995, **15**, 501–506.
36 D. Fan, P. Tian, S. T. Xu, Q. H. Xia, X. Su, L. Zhang, Y. Zhang, Y. L. He and Z. M. Liu, *J. Mater. Chem.*, 2012, **22**, 6568–6574.
37 K. Fujii, S. Hayashi and H. Kodama, *Chem. Mater.*, 2003, **15**, 1189–1197.
38 Z. L. Peng and X. J. Wu, *Fine Chemicals*, 2006, **23**, 873–877.
39 W. L. Shen, X. Li, Y. X. Wei, P. Tian, F. Deng, X. W. Han and X. H. Bao, *Microporous Mesoporous Mater.*, 2012, **158**, 19–25.
40 T. M. Suzuki, T. Nakamura, E. Sudo, Y. Akimoto and K. Yano, *J. Catal.*, 2008, **258**, 265–272.
41 Z. T. Xue, J. H. Ma, W. M. Hao, X. Bai, Y. H. Kang, J. H. Liu and R. F. Li, *J. Mater. Chem.*, 2012, **22**, 2532–2538.
42 H. Xue, Z. H. Li, H. Dong, L. Wu, X. X. Wang and X. Z. Fu, *Cryst. Growth Des.*, 2008, **8**, 4469–4475.
43 L. Guo, X. J. Bao, Y. Fan, G. Shi, H. Y. Liu and D. J. Bai, *J. Catal.*, 2012, **294**, 161–170.
44 K. Liu, H. P. You, G. Jia, Y. H. Zheng, Y. J. Huang, Y. H. Song, M. Yang, L. H. Zhang and H. J. Zhang, *Cryst. Growth Des.*, 2010, **10**, 790–797.
45 G. Y. Liu, P. Tian and Z. M. Liu, *Chin. J. Catal.*, 2012, **33**, 174–182.
46 D. Chen, K. Moljord, T. Fuglerud and A. Holmen, *Microporous Mesoporous Mater.*, 1999, **29**, 191–203.
47 Z. B. Li, J. Martinez-Triguero, P. Concepcion, J. H. Yu and A. Corma, *Phys. Chem. Chem. Phys.*, 2013, **15**, 14670–14680.
48 H. Fu, W. G. Song and J. F. Haw, *Catal. Lett.*, 2001, **76**, 89–94.
49 J. F. Haw, W. G. Song, D. M. Marcus and J. B. Nicholas, *Acc. Chem. Res.*, 2003, **36**, 317–326.

